Available online at www.sciencedirect.com
SCIENCE DIRECT®
Journal of Sound and Vibration 274 (2004) 73–89
JOURNAL OF SOUND AND VIBRATION
www.elsevier.com/locate/jsvi

Dynamic modelling of mechanical systems with opposing restrained preloaded stiffnesses

R.J. Rogers*, P. Garland, M. Oliver[1]

Department of Mechanical Engineering, University of New Brunswick, P.O. Box 4400, Fredericton, NB, Canada

Received 25 April 2002; accepted 13 May 2003

Abstract

Preloaded springs are used in many mechanical systems such as suspension systems and linkages, as well as household items such as clothing clasps. Usually, the preload has no effect on small amplitude dynamic responses which occur about the mean preloaded position. However if the system has opposing preloaded elastic elements, where unloading is limited by restraints such as central rods which preserve the preload, then the preload has a dramatic effect on a system's dynamic response. When such a system is set into free oscillation, the period of motion steadily decreases as the amplitude diminishes. Until now the authors have not seen this behavior described elsewhere.

The present work is motivated by the modelling of joysticks which are used to actuate hydraulic systems in a wide variety of mobile construction and forestry equipment. Their use for long periods of time may lead to repetitive strain injuries in an operator's upper limbs, neck and back. In order to assess the total force required to move a joystick, the stiffness, damping and inertia characteristics must be determined. A mathematical model for joystick dynamics is presented and the effect of restrained spring preloads on the changing period of free vibration is explained. In addition, procedures to estimate the non-symmetric non-linear damping from experimental data are described. By simulating the dynamic response in MATLAB™, the damping is fine-tuned by comparing the joystick's simulated free oscillation response with its experimental response. Finally, the torque waveform required to perform a simple joystick motion is estimated. The methods developed in this paper could be applied to any lumped-parameter mechanical system where there are opposing restrained preloaded elastic elements.

*Corresponding author. Tel.: +1-506-453-4513; fax: +1-506-453-5025.
E-mail address: rjr@unb.ca (R.J. Rogers).
[1] Presently with the School of Engineering, University of Guelph, Guelph, Ontario, Canada

0022-460X/$ - see front matter © 2003 Elsevier Ltd. All rights reserved.
doi:10.1016/S0022-460X(03)00649-7

1. Introduction

In its simplest form, the idealized mechanical system under consideration is shown in Fig. 1. The system is similar to an impact pair [1] where the central mass may move through a small clearance space to make contact with massless damped springs. In this case, however, the central rod passing through each spring is designed (for example with threads), so that each spring may be given an initial compressive preload. The unloading of each spring is limited to this initial preload. The effect of the clearance in this system is relatively minor and could be zero. The primary emphasis in this paper is on the effect of the pair of restrained springs, which causes the period of free vibration to diminish as the amplitude of motion decreases. Also of interest are procedures used to estimate a non-linear damping model for such a system.

The system shown in Fig. 1 could represent a variety of applications. One could imagine such a system as a snubber for pipes or tubes or as components of an electrical switch. For small contact forces, the spring deflection would be negligible; large deflections would occur only when the contact force exceeds the compressive spring preload. In this way the cental mass would remain centered, unless a significant excursion from center is required.

The motivation for the present work is the study of joysticks used in North American mobile construction and forestry equipment to control the positions of various hydraulic actuators by controlling the flow of hydraulic fluid through servo-valves. Joysticks, such as the one shown in Fig. 2, have universal joints which permit rotation about two horizontal axes with a range of motion of about $\pm 20^\circ$. Under the swash plate (cam) there are four spring-loaded plungers with hemispherical heads. Each plunger is connected to a valve stem assembly having two preloaded helical springs. If the joystick is rotated about one axis, for example, one plunger is depressed a distance approximately proportional to the angle of rotation.

The machinery operator must exert force on the joystick to make it move. There may be 20,000 such moves in a typical operator's work shift [2]. It is thought that the use of joysticks over extended periods can lead to repetitive strain injuries in an operator's upper limbs, neck, and back [3]. The present study was part of an experimental study [4] of arm and joystick motions and the forces involved in joystick use. The experimental set-up is shown in Fig. 3.

The force required to move a joystick can be considered to have stiffness, damping and inertia-related terms. Characterizing the stiffness term requires quasi-static load–deflection measurements of the spring assembly. The inertia term requires measurement of the joystick mass, center of mass and mass moments of inertia. The assessment of the damping term is more difficult and requires dynamic experimental testing. For most mechanical systems, the damping can be estimated from its frequency response or from the logarithmic decrement method applied to its free vibration

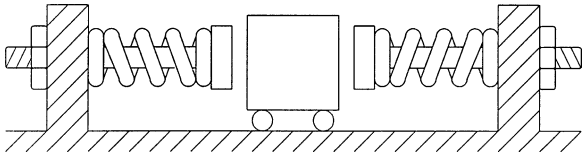

Fig. 1. Simple mechanical system with opposing restrained preloaded springs.

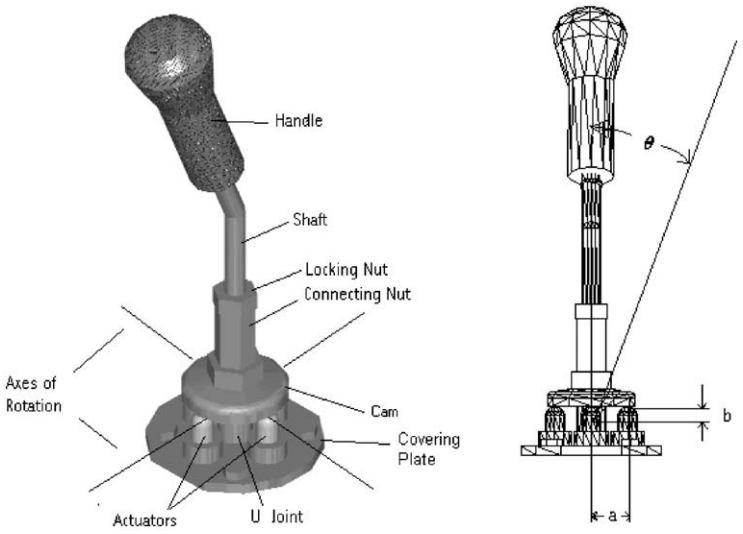

Fig. 2. Joystick geometry (boot removed).

Fig. 3. Subject and retroreflective marker placement in excavator cab/joystick mock-up.

response. For a joystick (or any system with opposing restrained preloaded springs), the large spring preloads result in its natural oscillation frequency being highly amplitude dependent so that traditional damping estimation methods cannot be used.

2. Free oscillation response

Typical joystick free oscillation behavior is illustrated by the angular displacement, velocity and acceleration time histories shown in Fig. 4. The right-hand joystick from a new excavator was initially held at its extreme backward position and then released. It was instrumented with two independent measurement systems. Small retroreflective balls were fastened to the joystick so that a 6-camera video VICON^{TM} imaging system could record the joystick's instantaneous position. The three-dimensional displacement data for each retroreflective ball were obtained at a sampling rate of 60 Hz.The positions of the ball at the top of the joystick and two balls on the base allowed vectors to be defined where x was horizontal and in the primary direction of motion, y was horizontal and perpendicular to the direction of motion, and z was vertical. The small y direction VICON results (2–3% of peak x motion) confirmed that the joystick motion was essentially planar. Using the x,z- projections of the vectors, the angular position of the joystick was found using a vector dot product. The angular displacement waveform was interpolated to give 600 Hz data point spacing and then digitally filtered, forward and reverse, through a low-pass fourth order Butterworth filter with a frequency cutoff at 13 Hz. The angular displacement waveform was then numerically differentiated using a 5-point rule to obtain the velocity waveform shown in Fig. 4(b). The angular acceleration waveform in Fig. 4(c) was obtained using a similar process with a 3-point rule. In addition, a small accelerometer (B&K Type 4393 V) was fastened to the front of the joystick near the top. Its signal was amplified by a charge amplifier (B&K Type 2635) and sampled at 1800 Hz. Its acceleration, divided by its distance to the universal joint pivot, is shown in Fig. 4(d).

Several features of the responses shown in Fig. 4 are striking. As expected, the signal amplitudes steadily decrease, however, untypical of most mechanical systems is the steady decrease in the

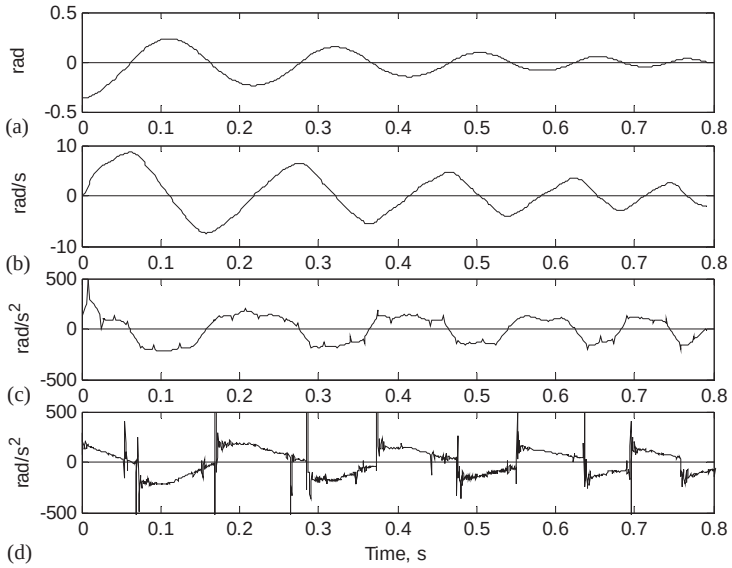

Fig. 4. Typical joystick angular responses during free oscillation: (a) displacement; (b) velocity; (c) VICON^{TM} acceleration; (d) accelerometer acceleration.

period of oscillation. This sort of behavior is more typical of bouncing balls or objects rocking about their edges [5,6], although in this case damping occurs throughout the motion rather than due only to a coefficient of restitution at each impact. The pattern of pairs of peak values in Fig. 4(a) is interesting. For example, the first positive and first negative full peaks have nearly the same amplitude. This pattern appears to repeat for subsequent pairs of peaks. This implies that the stiffness and/or damping are not exactly the same on the two sides. Also interesting are the portions of nearly constant acceleration and consequently nearly constant velocity slopes during each period of free motion.

The spikes in the acceleration from the accelerometer (see Fig. 4(d)) are due to the small impacts as the joystick passes through the neutral position and the plungers stop and start moving on each side. The spikes in the accelerometer data and the high-frequency ringing shown in Fig. 4(d) corrupt the acceleration signal, so that integrating results in invalid velocity and displacement waveforms. Also the changing orientation of the accelerometer introduces a small gravity acceleration component along the axis of the accelerometer [7], which also introduces errors into its velocity and displacement waveforms. The gravity component is maximum at the extreme joystick positions and has been estimated to be about 6% of the peak acceleration.

Despite the instrumentation limitations, it is clear that the free oscillation behavior of this single-degree-of-freedom system with opposing restrained preloaded springs is rather complex. There appears to be little literature on the effect of restrained preloaded springs. Chen and Chang [8] considered the frequency response of a preloaded single-degree-of-freedom system but the springs were not restrained to maintain their preloads, so that the effect of decreasing period is not observed. Johnson et al. [9] consider the effect of spring preloads in the touch trigger probes on the error characteristics of coordinate measuring machines (CMMs).

In the present paper, the effect of restrained spring preloads on the changing period of free vibration is explained and procedures to estimate the non-linear damping from experimental waveforms (such as Fig. 4) are described. A mathematical model for the joystick dynamics is presented. By simulating the transient response of the joystick in MATLAB^{TM}, the damping is fine-tuned by comparing the joystick's simulated free oscillation response with its experimental response. An error analysis shows the preferred damping values, as well as the sensitivity of the system to different damping values. Finally, using displacement data for a typical forward and return joystick motion by an operator, the components of the required torque waveform are estimated. The methods developed in this paper could be applied to any lumped-parameter mechanical system with opposing restrained preloaded elastic elements.

3. System model

The equation of planar motion for a joystick in free oscillation is obtained by summing the moments about the pivot as shown in the free body diagram in Fig. 5 and equating the external torques to the product of the mass moment of inertia J and the angular acceleration. The equation of motion is given by

$$J\ddot{\theta} + C\dot{\theta} + M_s = mgh \sin\theta, \tag{1}$$

where θ is measured from the neutral position, J is the mass moment of inertia about the pivot, C is the damping coefficient or damping function, M_s is the moment caused by the contact force at

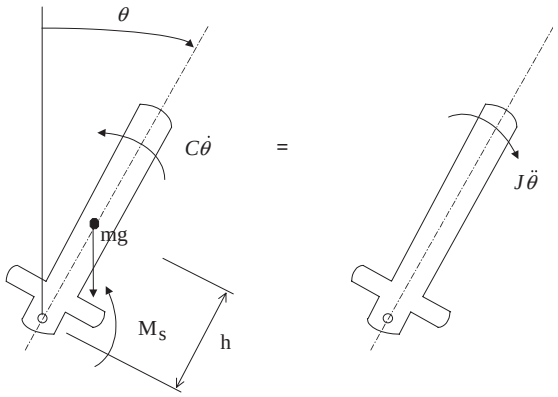

Fig. 5. Joystick free body diagram.

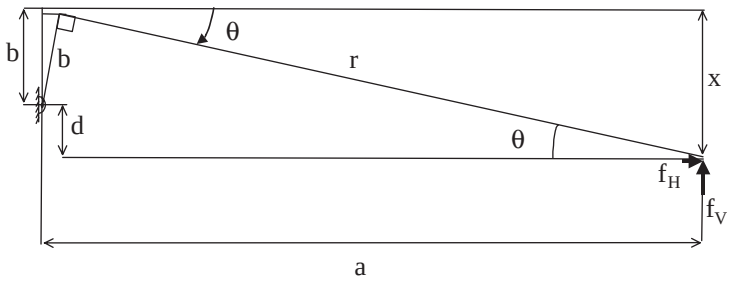

Fig. 6. Geometry and contact forces on joystick cam plate.

either plunger, m is the joystick mass, g is the acceleration of gravity and h is the height of the center of mass above the pivot.

As the cam surface rotates about the pivot, the point of contact with the actuator moves along the surface. The essential geometry and the two components of the normal contact force, f_H and f_V are shown in Fig. 6, where the actuator is treated as a contact point and its curvature is neglected. The contact friction force is not calculated explicitly; instead, all friction forces and moments are treated as sources of energy dissipation and are lumped into the damping term of Eq. (1). The fixed length a is the distance from the pivot center to the axis of each actuator assembly and b is the vertical distance from the pivot center to the lower cam surface; a and b are illustrated in Fig. 2. The distance x is the total deflection of the spring assembly plus any clearance. The horizontal and vertical components of r are given by

$$r\cos\theta = a - b\sin\theta, \quad r\sin\theta = x - b + b\cos\theta. \tag{2a, b}$$

Solving for x gives

$$x = a|\tan\theta| + b(1 - 1/\cos\theta), \tag{3}$$

where for convenience x is taken as positive for any θ. The moment M_s is defined by the moments of the components of the normal contact force, f_V and f_H, about the pivot,

$$M_s = af_V + df_H, \tag{4}$$

where the moment arm of f_H is $d = x - b$. Noting that $f_H = f_V \tan\theta$, where f_V is the force acting on the spring assembly f_x, and accounting for the sign change of the af_V term in Eq. (4) gives the final form for the actuator moment which is valid for any θ:

$$M_s = \{a\,(\text{sign}(\theta) + d\,\tan\,\theta\}f_x \tag{5}$$

3.1. Preloaded stiffness modelling

Fig. 7(a) schematically shows the arrangement of an actuator plunger and its balance and return springs. Its typical static load–deflection behavior shown in Fig. 7(b) was measured using an Instron™ testing machine. The actual load–deflection curve has two very steep portions and two gradually rising portions. The initial steep slope is due to the compressive preload in the return spring. The applied force f_x must overcome the large preload in the return spring before any significant deflection occurs. After about 3 mm displacement, the actuator rod bottoms out and the second steep slope shows that the preload in the balance spring must then be overcome. In the final stage, the effective stiffness is the sum of the two spring stiffnesses. The overall stiffness of the system clearly decreases with increasing compression distance. A fitted cubic polynomial curve has also been plotted in Fig. 7(b) in order to illustrate this reduction in system stiffness.

The effect of the compressive preloads on the load–deflection curve is similar to that of a bolted joint, whose behavior depends on both the stiffness of the bolt and the stiffness of the clamped material [10]. For example, as the pressure increases in a pressure vessel with a properly designed bolted–on head, the bolt tension will increase slightly, but the compression force in the clamped material will diminish much more, since its stiffness is much greater than that of the bolt. Bolted joint failure occurs when the compression of the clamped material becomes zero and the joint opens. The spring system shown in Fig. 7(a) operates under the same principles, but unlike a bolted joint, in this case the stiffer material is in tension and the desired behavior occurs when the joint opens.

Fig. 8(a) illustrates the load condition in the preloaded return spring when there is no external force. The compressive force in the spring is balanced by an equal tensile force in the housing surrounding the assembly. Since the housing stiffness k_h is much greater than the spring stiffness k_s, the housing elongation x_{ho} is much less than the initial spring deflection x_{so}. When an actuator force f_x occurs, the tensile force in the housing rapidly decreases and the spring force increases slightly as illustrated in Fig. 8(b). The actuator, housing and spring forces are in equilibrium so that

$$f_{spring} = f_x + f_{housing}. \tag{6}$$

If f_x is less than the preload force, then it is related to the actuator displacement x by the sum of the housing and spring stiffnesses,

$$f_x = (k_h + k_s)x. \tag{7}$$

When $k_h x$ exceeds the preload, the tensile force in the housing becomes zero, and the actuator force is simply given by

$$f_x = k_s(x_{so} + x). \tag{8}$$

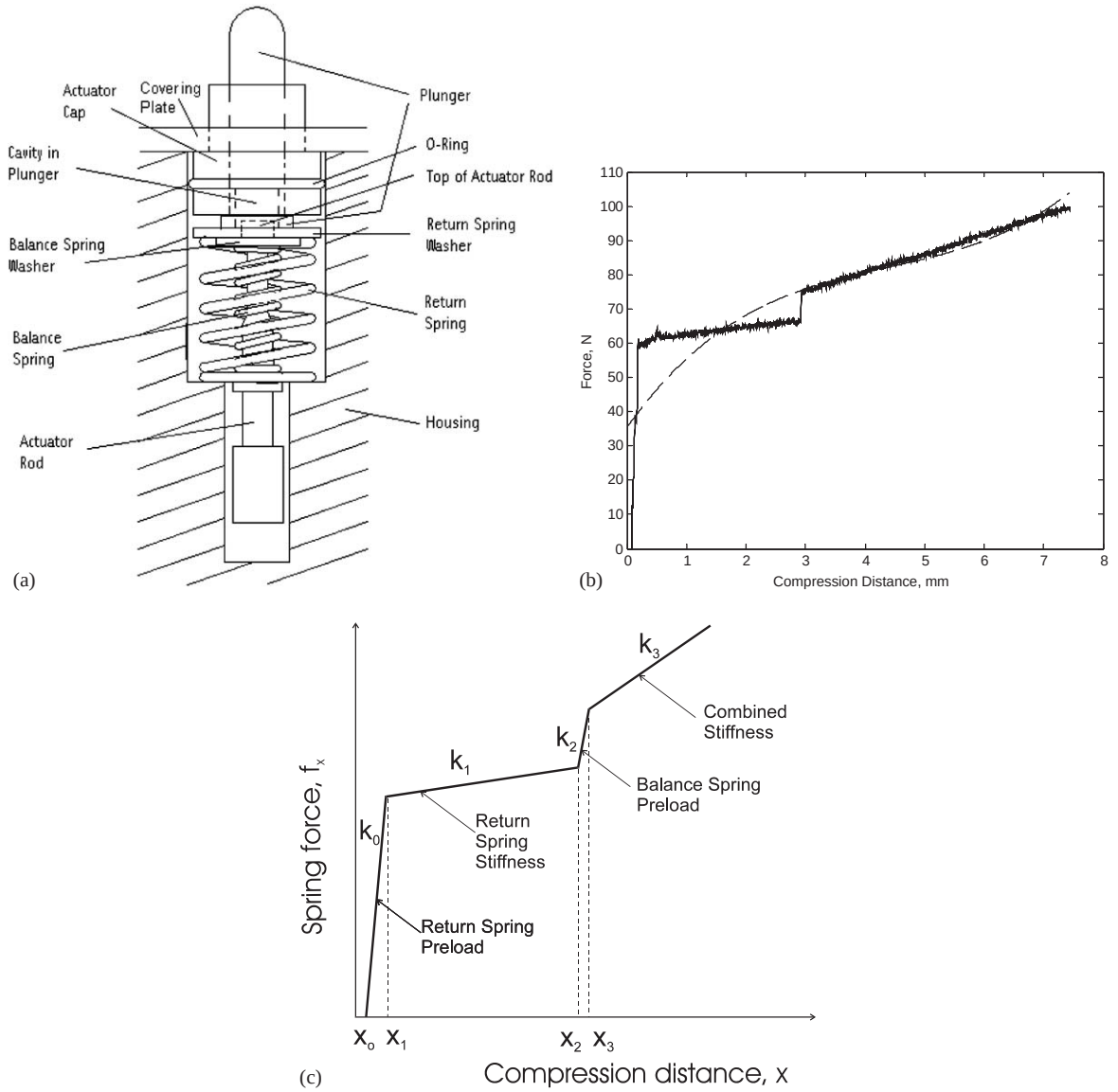

Fig. 7. Actuator springs: (a) dual-spring valve system; (b) typical measured load–displacement curve: Instron test data (solid); cubic polynomial fit (dashed); (c) spring force profile.

Large deflections can now occur for small increases in actuator force. A similar behavior occurs when the actuator rod bottoms out and the tensile force in the rod due the compressive preload in the balance spring must be overcome.

The piece-wise continuous load deflection curve for each actuator assembly has been modelled as a series of four linear spring stiffnesses as shown schematically in Fig. 7(c). The clearance of 0.075 mm is exaggerated in the figure. The corresponding starting displacement and stiffness values are shown in Table 1. The spring preloads are very important to the response of the

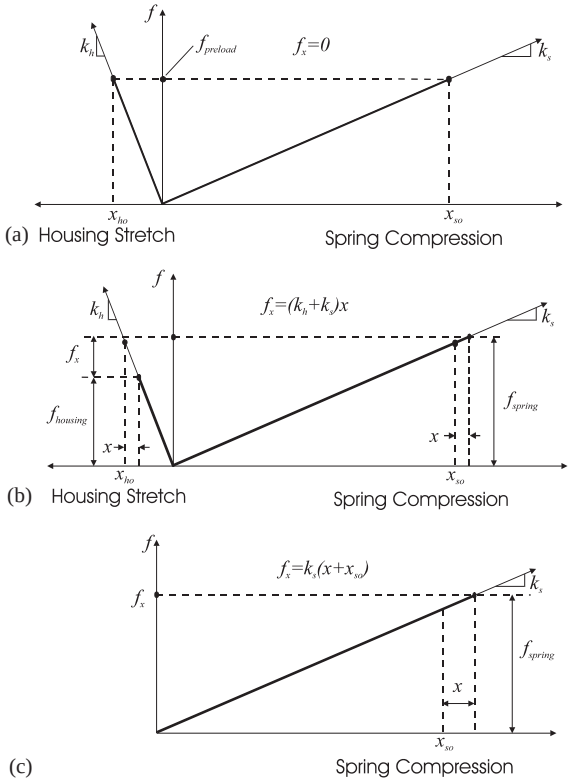

Fig. 8. Spring preload effects: (a) with no external force, f_x ; (b) when $f_x <$ spring preload; (c) when $k_h x >$ spring preload.

Table 1
Modelled spring displacements and stiffnesses

	Forward		Backward	
	Displacement	Stiffness	Displacement	Stiffness
i	x_i (mm)	k_i (N/m)	x_i (mm)	k_i (N/m)
0	0.075	430,000	0.075	659,000
1	0.1985	2625	0.1595	1191
2	2.932	1,028,000	3.054	1,112,000
3	2.943	5600	3.063	4090

actuator system and cause the interesting decreasing period during free vibration. As the oscillation amplitude decreases, the average stiffness of the system increases, giving a higher natural frequency. The lower stiffness values in the backward direction shown in Table 1 contribute to the larger than expected negative angular displacement peaks shown in Fig. 4(a).

Table 2
Joystick inertia and geometrical constants

Joystick mass	0.87 kg
Mass moment of inertia	0.01135 kg m^2
Pivot to center of mass	8.2 cm
Pivot to top	26.6 cm
Pivot to plunger contact (a)	23.98 mm
Pivot to cam surface (b)	5.0 mm

3.2. Inertia values

The mass moment of inertia of the joystick about its pivot was calculated from its geometry and also measured experimentally using a simple swing test. The latter was done by inverting the joystick and supporting it at the pivot. Its natural period of motion was obtained using a stopwatch. By modelling the inverted joystick as a compound pendulum, J is given by $mgh/(2\pi f_n)^2$, where f_n is the pendulum swing frequency. The mass and mass moment of inertia of the joystick handle are shown, along with other geometrical constants, in Table 2.

3.3. Non-linear damping modelling

There are several sources of damping in the joystick during free oscillation. Oil in the universal joint, between the plunger tips and the swash plate, and between the plungers and their guide walls should result in viscous damping. There is also some air-resistance damping. Viscous damping would tend to cause exponentially decreasing displacement amplitudes, whereas dry Coulomb friction damping would cause linearly decreasing peaks [11]. For the present case where the period of oscillation decreases, this effect is difficult to judge. Since the damping is expected to play a secondary role in the torque waveform and also for convenience, a viscous type of damping is assumed. Separate estimates of damping for positive and negative motions are needed, which precludes the use of the Hilbert transform to estimate the damping.

For a linear system with viscous damping and no preloaded springs, the envelope of the damped free response would be a simple exponential decay function and the peak angle values and peak times would be related by

$$|\theta_{peak}| = \theta(0)\, e^{-\xi\omega_n t_{peak}}, \tag{9}$$

where $\theta(0)$ is the starting angular position at time zero. The exponential decay argument $\xi\omega_n$ is $C/(2J)$ for a simple linear rotational system. Although Eq. (9) is based on a constant natural frequency, it will be used here to extract experimental estimates of C. By substituting experimental values of θ_{peak} and t_{peak}, estimates for C can be obtained by rearranging Eq. (9).

$$C_{exp} = -\frac{2J}{t_{peak}} \ln\left(\frac{|\theta_{peak}|}{\theta(0)}\right). \tag{10}$$

By plotting C_{exp} and θ_{peak} values from data such as shown in Fig. 4(a) on log–log scales, best fit straight lines for the positive and negative peaks provide functions of the form $C_{exp} = A|\theta_{peak}|^n$. Since this function allows the damping to vary with response amplitude, it is assumed that this

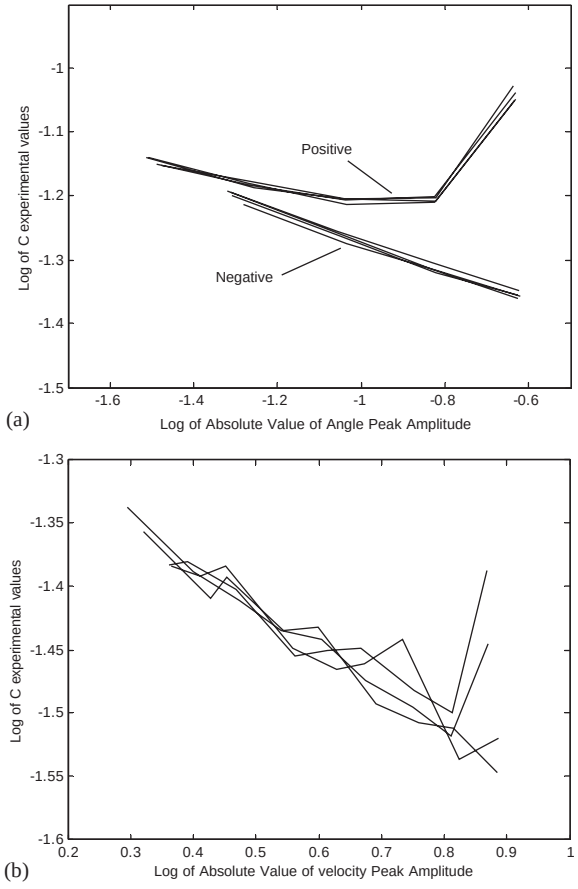

Fig. 9. Log of C_{exp} vs. log of peak heights: (a) angular position; (b) angular velocity.

expression could be used for the continuous functions $C_{exp}(\theta) = A|\theta|^n$. Since different actuator assemblies are involved for positive and negative values of θ, different values of A and n are used for positive and negative values of θ. A similar approach can be used with the angular velocity data shown in Fig. 4(b), giving the expression $C_{exp}(\dot{\theta}) = B|\dot{\theta}|^m$. Since the displacement and velocity expressions each account for all the damping, if they are combined, the A and B coefficients must be multiplied by weighting coefficients, i.e.,

$$C_{exp}(\theta, \dot{\theta}) = \alpha A|\theta|^n + \beta B|\dot{\theta}|^m, \tag{11}$$

where $\alpha + \beta = 1$.

The log–log plots for four data sets shown in Fig. 9 indicate fairly good straight line approximations with slight negative slopes, except for the highest abscissa values. The results in Fig. 9(a) indicate that for the particular joystick tested, there is more damping for positive θ than for negative θ and, except for the highest peaks, the damping tends to increase slightly as the amplitude of oscillation decreases. Unlike the displacement data, the velocity data for positive and negative θ overlap, as shown in Fig. 9(b), so that the same values of B and m may be used for all the velocity peaks. For simplicity, linear regression was used and gave the following coefficients

for Eq. (11): $A_{pos} = 0.086\,\text{N ms}$, $n_{pos} = 0.084$, $A_{neg} = 0.032\,\text{N ms}$, $n_{neg} = -0.23$, $B = 0.051\,\text{N ms}$ and $m_{neg} = -0.26$. Note that the negative values of the exponents, n and m, can lead to very high values of C_{exp} when either the angular displacement or angular velocity approach zero. The relatively low fractional exponents also suggest that a constant value of damping coefficient may give satisfactory results.

4. Simulation results and error analyses

In order to obtain a solution to Eq. (1), programs [4,12] were written in MATLAB^{TM} using fourth order Runge–Kutta numerical integration. Initial position and velocity values were taken as the average experimental values shortly after release. A small constant time step of 0.001 s was used, except near the steep slopes in the load–deflection curve, where the time step was divided by 10. Various values for weighting factors, α and β, were tried and compared with the measured responses of Fig. 4(a) and (b).

Fig. 10 shows typical simulation waveforms for $\alpha = 0.9$ and $\beta = 0.1$, along with one set of experimental waveforms. Also shown are simulation results with a constant damping coefficient $C = 0.045\,\text{N ms}$. By inspection, both simulations match the form of the experimental waveforms quite well. The characteristic decrease in oscillation period is shown quite well. The simulated velocity waveforms have sharper peaks than the experimental velocity waveforms obtained by differentiating the VICON^{TM} displacement waveforms.

Error analyses were performed in order to find the optimum values for α and β (or for constant C). Since the waveforms have both decreasing amplitude and decreasing period, the following

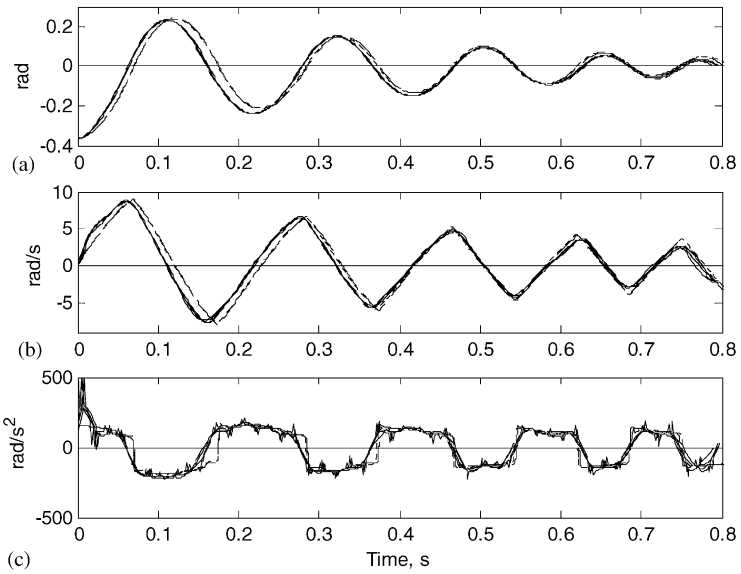

Fig. 10. Typical joystick free motion angular responses: (a) displacement; (b) velocity; (c) acceleration. Experimental (solid), simulation with damping function (long dashes), and simulation with constant for $C = 0.045$ (short dashes).

average relative errors were defined for the peak angular displacement values and the times at which they occurred:

$$\varepsilon_{disp} = \frac{1}{n}\sum_{i=i}^{n}\frac{|y_i - \hat{y}_i|}{\hat{y}_i}, \quad \varepsilon_{time} = \frac{1}{n}\sum_{i=i}^{n}\frac{|t_i - \hat{t}_i|}{(\hat{t}_i - \hat{t}_{i-1})}, \tag{12a, b}$$

where y_i and $\hat{y}_i$ are the ith simulated and experimental peak angular displacements occurring at times t_i and $\hat{t}_i$, respectively. The experimental values are the averages of four trials. Nine peaks ($n = 9$), including both positive and negative peaks, were used. A similar process was used to estimate the errors in the velocity waveforms with $n = 10$. These relative errors may be expressed as percentages by multiplying by 100.

Fig. 11(a) shows how these relative errors for peak angular data vary with α for the nonlinear damping and Fig. 11(b) shows the errors for various values of constant damping. From the displacement waveforms, the minimum peak-time error is 5.1% for $\alpha = 0.9$, while the peak-

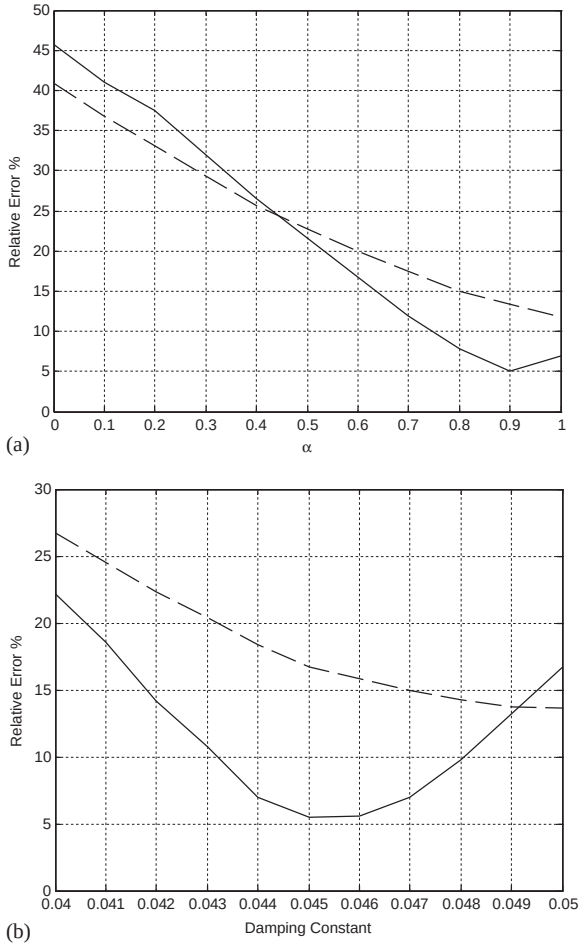

Fig. 11. Error in peak angular data: (a) for different α values; (b) for various values of constant damping. Peak time error (solid), peak displacement error (dashed).

displacement error has a minimum of 11.9% for $\alpha = 1$. Similarly for constant damping shown in Fig. 11(b), the minimum peak-time error is 5.4% for $C = 0.045$, while the minimum peak-displacement error is 13.6% for $C = 0.050$. All of these errors are quite small which demonstrates that the simulations match the experimental waveforms quite well. Similar trends and values were obtained for the errors in the velocity waveforms. The error results show the simulation error is not very sensitive to the choice of damping model and that even the constant damping works quite well.

As a verification of the mathematical model, the total energy of the system was calculated during the simulations. The gradual decay of total energy with time is shown in Fig. 12 for $\alpha = 0.9$. The total energy decreases in steps with the plateaus corresponding to times near zero velocity and therefore low damping. Fig. 12 also shows the estimated total energy using the experimental data. Although somewhat similar to the simulation energy, the experimental curve shows rises in energy which are physically impossible. This effect is due to underestimation of the peak experimental velocity and kinetic energy values because of limitations in the numerical differentiation of the displacement waveforms.

Finally, in order to see the discontinuities in the damping function given in Eq. (11), it has been plotted against time in Fig. 13. The largest discontinuities occur at the times of zero velocity and small discontinuities occur when the displacement is zero. It is interesting that these discontinuous damping coefficient values appear to have very little effect on the simulation. One can also see that the constant damping value of 0.045 N ms approximates an average value for the damping function.

5. Application

When a subject such as shown in Fig. 3 moves the joystick, the subject must exert a force on it. The resulting torque acting on the joystick can be modelled by introducing a torque T to the right hand side of Eq. (1) and then solving for T,

$$T = J\ddot{\theta} + C\dot{\theta} + M_s - mgh \sin\theta. \tag{13}$$

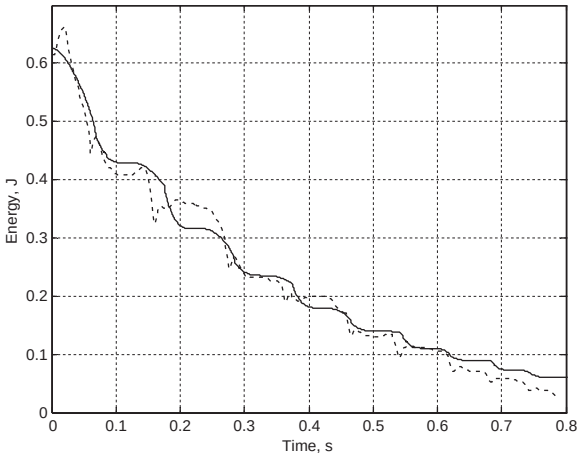

Fig. 12. Time history of system energy: simulation (solid), experimental (dashed).

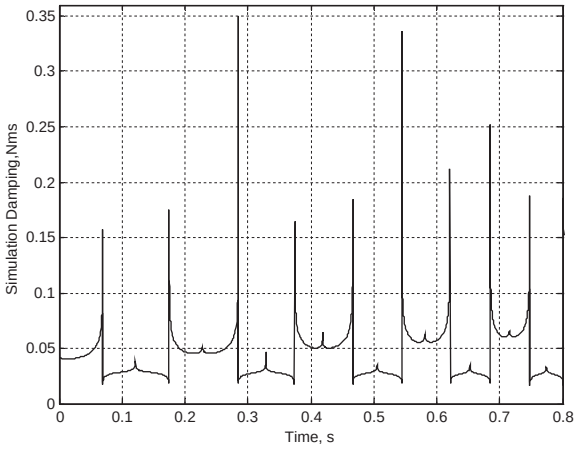

Fig. 13. Time history of equation (11) damping function showing discontinuities.

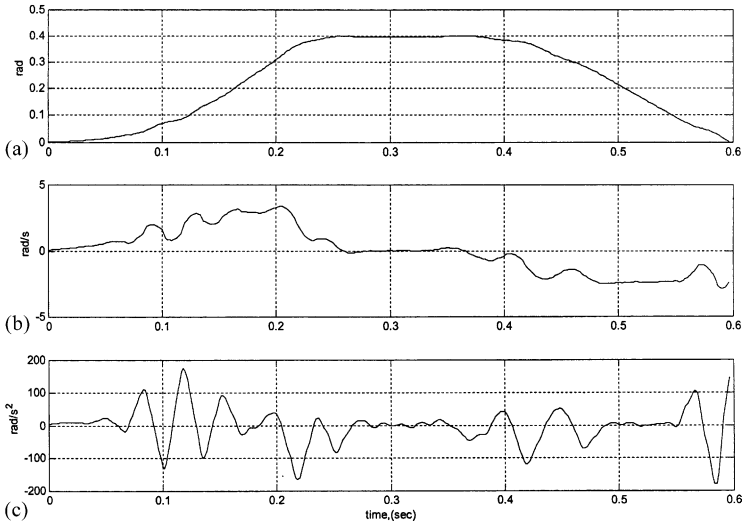

Fig. 14. Forced joystick angular motions: (a) displacement; (b) velocity; (c) acceleration.

In order to see the influence of each term in the equation, a typical displacement waveform for simple forward and return motion by a subject was obtained using the VICON^{TM} camera system [4]. The velocity and acceleration waveforms were then obtained as described earlier in this paper. The resulting waveforms are shown in Fig. 14. Although the displacement waveform appears quite smooth, the velocity and acceleration waveforms show some oscillation.

By substituting these waveform values into the acceleration, velocity and displacement-related terms in Eq. (13), the resulting torque components were calculated and are shown in Fig. 15. The main contributors to the total torque, shown in Fig. 15(d), are the stiffness ($M_s - mgh \sin\theta$) and inertia related terms. The damping torque values shown in Fig. 15(b) are relatively small (roughly

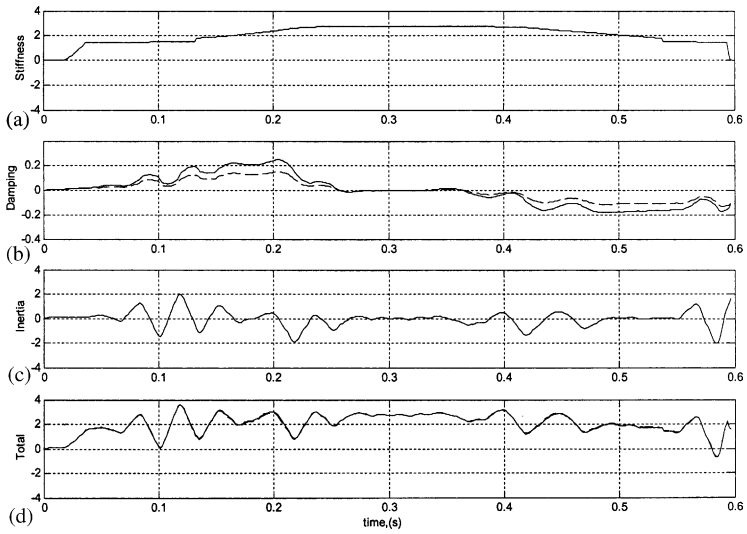

Fig. 15. Torque components for force motion: (a) stiffness; (b) damping: with damping function (solid), with constant $C = 0.045$ (dashed); (c) inertia; (d) total.

10%). It is interesting to see that the nonlinear damping model gives roughly double the damping torque compared to the constant damping model (dashed curve).

6. Conclusions

The stiffness, damping and inertia characteristics of a mechanical system with opposing restrained preloaded springs have been modeled. A joystick, which is used to actuate hydraulic systems in a wide variety of mobile construction and forestry equipment, has been used as an illustrative system since knowledge of its stiffness, damping and inertia characteristics enable studies of actuation forces by human operators to be conducted.

The restrained preloaded springs allow for minimal deflection until the applied force exceeds the spring preload. The interaction of the housing (or rod) stiffness and the helical spring stiffness is shown to be conceptually similar to a bolted joint. The restrained preloaded springs are responsible for the decreasing period during decaying free vibration, since as the amplitude of motion decreases, the average stiffness becomes higher.

A simple method has been used to estimate amplitude-dependent damping which allows for different stiffness and damping properties for positive and negative motions. Weighted non-linear dependencies on angular displacement and velocity are used.

The simulation results show that the mathematical model can represent both the decreasing amplitude and decreasing oscillation period quite well, demonstrating that the model accurately represents the essential characteristics of the system. Error analyses of the angular displacement peak values and their occurrence times enabled optimum values of damping weightings to be obtained. Although the simulation is not especially sensitive to the choice of the damping model,

the best results are obtained when damping proportional to angular displacement is dominant, with very similar results being obtained with constant damping.

Using a displacement waveform generated by a subject for simple forward and return motion, velocity and acceleration waveforms were generated and the corresponding components of the torque applied to the joystick were produced. The results showed that for this case, the inertia torque was comparable in size to the displacement-related torque and that the damping torque was much smaller and of the order of 10% of the total torque.

Although this paper discusses a hydraulic actuation joystick, the analysis and methods could be applied to any system with opposing restrained preloaded springs.

Acknowledgements

The authors wish to thank the University of New Brunswick, especially the Institute of Biomedical Engineering, for enabling this work to be done. Special thanks go to Professors Ed Biden and Jeremy Rickards, as well as PhD student, Vicky Chester, for her help with the new VICON system and BScE student, Troy Gallant, for his initial work on this problem.

References

[1] S. Dubowsky, F. Freudenstein, Dynamic analysis of mechanical systems with clearances, Part 1: formation of dynamic model, *Journal of Engineering for Industry* 93 (1971) 305–316.

[2] J.-M. Golsse, Forest Engineering Research Institute of Canada-Wood, Harvesting , Technical Note TN-134, 1989

[3] M.L. Oliver, E.J. Rickards, E.N. Biden, Off-road machine controls: investigating the risk of carpal tunnel syndrome, *Ergonomics* 43 (2000) 1887–1903.

[4] M.L. Oliver, Joystick Dynamics and the Effects of Stiffness and Speed on Upper Limb Kinematics, PhD Dissertation, Department of Mechanical Engineering, University of New Brunswick, 2001.

[5] C.-S. Yim, A.K. Chopra, J. Penzien, Rocking response of rigid blocks to earthquakes, *Earthquake Engineering and Structural Dynamics* 8 (1980) 565–587.

[6] S.C.S. Yim, H. Lin, Nonlinear impact and chaotic response of slender rocking objects, *Journal of Engineering Mechanics* 117 (1991) 2079–2101.

[7] K.G. McConnell, *Vibration Testing: Theory and Practice*, Wiley, Toronto, 1995, pp. 164–169.

[8] F.Y. Chen, R.Y. Chang, Dynamic response characteristics of contact separation in a preloaded mechanical joint, *ASME Design Engineering Technical Conference*, Minneapolis, Paper 78-DET–48, 1978.

[9] R.P. Johnson, Q. Yang, C. Butler, Dynamic error characteristics of touch trigger probes fitted to coordinate measuring systems, *IEEE Transactions on Instrumentation and Measurement* 47 (1998) 1168–1172.

[10] R.L. Norton, *Machine Design—An Integrated Approach*, 2nd Edition, Prentice-Hall, Upper Saddle River, NJ, 2000.

[11] W.T. Thompson, M.D. Dahleh, *Theory of Vibration with Applications*, 5th Edition, Prentice-Hall, Upper Saddle River, NJ, 1988.

[12] P. Garland, Modeling the dynamic response of hydraulic actuating joysticks, Mechanical Engineering Senior Report, University of New Brunswick, 2001.